 doi:10.20944/preprints202204.0041.v1

Article

Magnetoliposomes Containing Multicore Nanoparticles and A New Thienopyridine Antitumor Compound for Chemo/Thermotherapy

Fábio A. C. Lopes[1,2], André V. F. Fernandes[1,2], Juliana M. Rodrigues[3], Maria-João R. P. Queiroz[3], Bernardo G. Almeida[1,2], Ana Pires[2,4], André M. Pereira[2,4], João P. Araújo[2,4], Ana Rita O. Rodrigues[1,2], Elisabete M. S. Castanheira[1,2,*] and Paulo J. G. Coutinho[1,2,*]

[1] Physics Centre of Minho and Porto Universities (CF-UM-UP), University of Minho, Campus de Gualtar, 4710-057 Braga, Portugal; pg40847@alunos.uminho.pt (F.A.C.L.); pg38822@alunos.uminho.pt (A.V.F.F.); bernardo@fisica.uminho.pt (B.G.A.); ritarodrigues@fisica.uminho.pt (A.R.O.R.)
[2] LaPMET (Laboratory of Physics for Materials and Emergent Technologies), Associate Laboratory, Portugal
[3] Centre of Chemistry (CQUM), University of Minho, Campus de Gualtar, 4710-057 Braga, Portugal; juliana.mourarodrigues@gmail.com (J.M.R.); mjrpq@quimica.uminho.pt (M.-J.R.P.Q.)
[4] IFIMUP—Instituto de Física dos Materiais, Universidade do Porto, R. Campo Alegre, 4169-007 Porto, Portugal; ana.pires@fc.up.pt (A.P.); ampereira@fc.up.pt (A.M.P.); jearaujo@fc.up.pt (J.P.A.)
* Correspondence: ecoutinho@fisica.uminho.pt (E.M.S.C.); pcoutinho@fisica.uminho.pt (P.J.G.C.)

Abstract: Multicore magnetic nanoparticles of manganese ferrite were prepared using carboxymethyl-dextran and melamine as agglutinating agents. The nanoparticles prepared using melamine exhibit a flower-shape structure, a saturation magnetization of 6.16 emu/g and good capabilities for magnetic hyperthermia. Magnetoliposome-like structures containing the multicore nanoparticles exhibit sizes in the range 250 – 400 nm. A new antitumor thienopyridine derivative was loaded in these nanocarriers with a high encapsulation efficiency of 98% ± 2.6%. Release profiles in absence and presence of an AMF indicate a transport by diffusion, with a maximum compound release of 31% under the AMF. A sustained and controlled drug release in anticipated from the results, pointing to suitable characteristics of the magnetoliposomes for dual cancer therapy (combined magnetic hyperthermia and chemotherapy).

Keywords: multicore magnetic nanoparticles; magnetoliposomes; magnetic hyperthermia; antitumor thienopyridine derivative; chemotherapy

1. Introduction

According to the International Agency for Cancer Research, in 2018 there were 18.1 million new cancer cases and nearly 10 million cancer-related deaths [1]. It is estimated that one in six deaths worldwide is due to cancer, emphasizing the need of local and efficient nanotherapeutics.

In recent years, magnetic nanoparticles have shown promising results for cancer therapy using magnetic hyperthermia, while being used in cancer diagnosis through magnetic resonance imaging (MRI). Furthermore, it is possible to guide the nanoparticles with a magnetic field gradient, so it is possible to achieve a controlled release of drugs at specific tumor locations using drug-loaded magnetic nanoparticle-based systems [2,3]. Superparamagnetic behavior is also an important feature in magnetic nanoparticles for therapy, because no magnetization remains after removal of the applied alternating magnetic field [4]. Magnetic nanoparticles with a flower-like multicore structure have shown enhanced magnetic hyperthermia capabilities, with high magnetic resonance relaxivity and high specific absorption rate (SAR) when an AC magnetic field is applied, evidencing improved performance as cancer theranostic agents [5,6]. The typical size of the constituent particles of multicore nanostructures is around 10 nm, forming aggregates

Preprints (www.preprints.org) | NOT PEER-REVIEWED | Posted: 6 April 2022 doi:10.20944/preprints202204.0041.v1

from 20 to 80 nm [6]. This translates into a weak magnetization (lower than that of the particles forming the aggregate) and a consequent low tendency to form agglomerates of larger dimensions, an important feature for biomedical applications [6,7].

Considering these properties, the development of magnetoliposomes containing multicore magnetic nanoparticles allows preserving their magnetic properties and hyperthermia capability [8], while providing suitable drug carriers with increased biocompatibility, flexibility in composition and size, improved drug pharmacokinetics, and prolonged circulation in vivo [9,10]. Particularly, solid magnetoliposomes (nanoparticles covered by a lipid bilayer) containing manganese ferrite nanoparticles have shown similar saturation magnetization as the neat nanoparticles, while being especially adequate for the transport of hydrophobic drugs [11].

In this work, a novel antitumor compound, a thieno[3,2-*b*]pyridine derivative (figure 1), was encapsulated in magnetoliposomes containing multicore manganese ferrite nanoparticles. This compound has shown a promising antitumor activity with low growth inhibitory concentrations (GI_{50}) in four tumor cell lines, namely in HeLa (cervical carcinoma; GI_{50} =12.99 ± 0.58 μM), MCF-7 (breast adenocarcinoma; GI_{50} =15.13 ± 0.59 μM), NCI-H460 (non-small cell lung carcinoma; GI_{50} = 12.60 ± 0.8 μM) and HepG2 (hepatocellular carcinoma; GI_{50} = 7.51 ± 0.48 μM) [12]. Moreover, the compound has shown a much lower cytotoxic effect in non-tumor cells PLP2 (Porcine Liver Primary cell line; GI_{50} = 95.94 ± 5.23 μM), being thus promising as a chemotherapeutic agent [12].

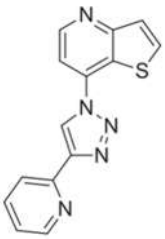

Figure 1. Chemical structure of the new antitumor compound.

With the motivation of achieving more effective and synergistic therapies through the combination of magnetic hyperthermia and chemotherapy, reducing the drug dosage needed by application of a local treatment, the nanosystems were evaluated for their potential of drug release and magnetic hyperthermia capabilities.

2. Materials and Methods

2.1. Synthesis of multicore manganese ferrite nanoparticles

2.1.1. Synthesis using carboxymethyl-dextran polysaccharide

The manganese ferrite ($MnFe_2O_4$) nanoparticles were prepared by co-precipitation, according to the procedure previously described [4]. The metallic precursors used in NPs synthesis were iron(III) chloride hexahydrate ($FeCl_3{\cdot}6H_2O$) and manganese sulfate monohydrate ($MnSO_4{\cdot}H_2O$), both from Sigma-Aldrich (St. Louis, MO, USA). Sodium hydroxide (NaOH, 50% in water) was used as hydroxylating agent, as previously described [4]. Carboxymethyl-dextran (Sigma-Aldrich, St. Louis, MO, USA) was employed as the agglutinating agent for the nanoparticles [5,6].

Two types of manganese ferrite nanoparticles (A1 and A2) were synthesized using carboxymethyl-dextran to promote the nanoparticles aggregation in a multicore structure [13]. The synthesis includes two steps that correspond to the production of manganese ferrite nanoparticles and the formation of the multinuclear structure by the presence of a polysaccharide. The synthesis methods differ only in the step of addition of the polysaccharide. In A1 nanoparticles, the polysaccharide is added after the synthesis of the nanoparticles, while, for A2, it is added before the synthesis of the nanoparticles (figure 2).

Preprints (www.preprints.org) | NOT PEER-REVIEWED | Posted: 6 April 2022 doi:10.20944/preprints202204.0041.v1

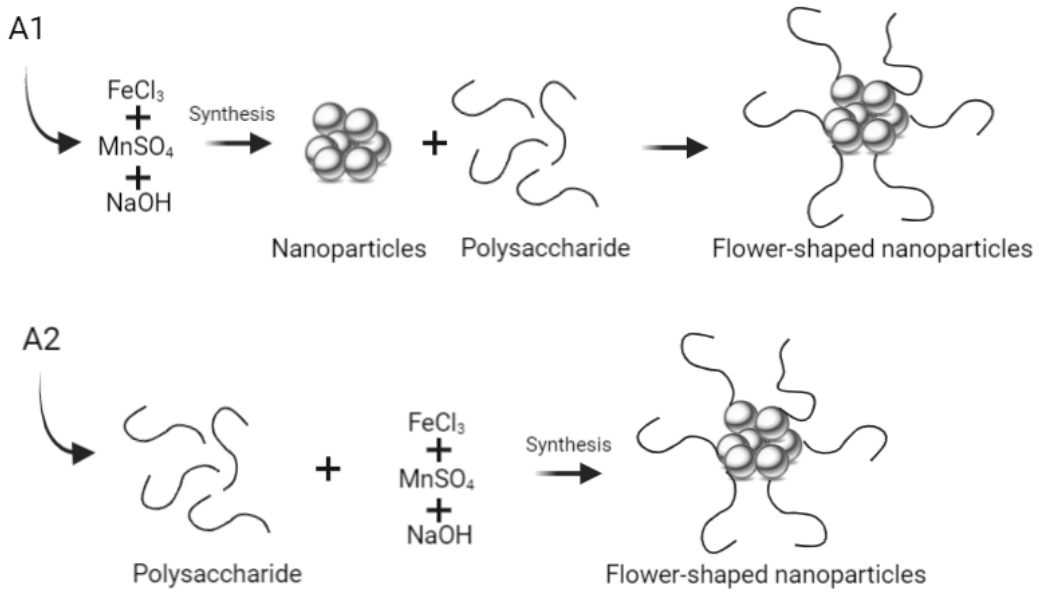

Figure 2. Schematic representation of the process of synthesis of multicore (flower-shaped) nanoparticles using the polysaccharide carboxymethyl-dextran.

First, a 19 mL aqueous solution containing 8 mmol of NaOH was heated to 100 °C in a volumetric flask. For A1 nanoparticles, $FeCl_3 \cdot 6H_2O$ (1.4 mmol) and $MnSO_4 \cdot H_2O$ (0.7 mmol) were added under magnetic stirring in 1 mL of deionized water. After 15 minutes, 100 mg of carboxymethyl-dextran was added. The solution was kept at 100 °C for two hours under magnetic stirring.

For A2 nanoparticles, the addition of 100 mg of carboxymethyl-dextran occurred before the addition of the metallic precursors (iron chloride and manganese sulfate), under the same stoichiometric ratio.

Finally, the obtained nanoparticles were washed with ethanol with several steps of washing and magnetic decantation.

2.1.2. Synthesis using melamine

In this method, the surface of the manganese ferrite nanoparticles was activated before the addition of the binding agent. For this, *N*,*N*'-carbonyldiimidazole (CDI) from FluoroChem (Derbyshire, UK), melamine and imidazole (Sigma-Aldrich, St. Louis, MO, USA) were used. Manganese ferrite NPs (4.3×10^{-5} mol) were dispersed in 7 mL of dry dimethyl sulfoxide (DMSO). Then, CDI (2.2×10^{-4} mol) was added, and the solution was kept at 60 °C under sonication for 2 hours. Ultrapure water was used to eliminate CDI excess and, after 15 minutes, melamine (4.3×10^{-5} mol) was added. Finally, after the addition of an equivalent quantity of imidazole (4.3×10^{-5} mol), the reaction was kept at 60 °C for two hours, under sonication. The use of imidazole allows a faster coupling of the $-NH_2$ groups of melamine to the -OH groups on the NPs surface that were activated by CDI in the previous step (figure 3) [14,15]. These nanoparticles will be designated as "B" in the subsequent work.

Preprints (www.preprints.org) | NOT PEER-REVIEWED | Posted: 6 April 2022 doi:10.20944/preprints202204.0041.v1

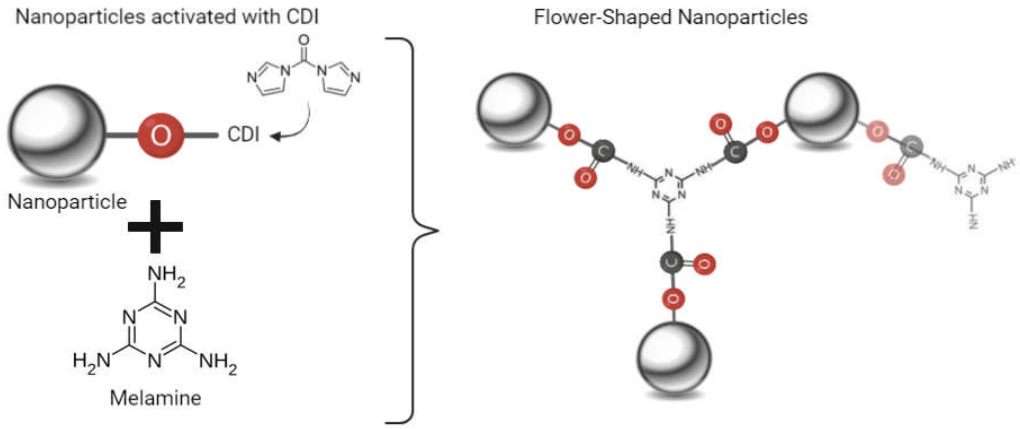

Figure 1. Schematic representation of the synthesis of flower-shaped nanoparticles using melamine (nanoparticles B).

2.2. Magnetoliposomes preparation

Magnetoliposome-type structures were prepared following a procedure already employed for manganese ferrite/gold nanoparticles [16]. A solution of multicore manganese ferrite nanoparticles (1×10^{-6} mol in 5 mL water) was placed in an ice bath under magnetic stirring, and 1.2×10^{-6} mol de CDI were added to activate surface groups. Then, octadecylamine (ODA) in a five-fold excess was added to the nanoparticles, and this solution was stirred for 1 h. The solution was washed with successive centrifugations and magnetic decantation to remove unbound ODA. After this step, an ethanolic solution of 1 mM DPPC (dipalmitoylphosphatidylcholine) was added to the nanoparticles covered with ODA. After evaporation of the solvent, a uniform lipid film was obtained and ultrapure water was added, followed by sonification to promote liposome formation. This procedure was followed by two washing steps, consisting of centrifugation and magnetic decantation.

To prove the liposome-like structure, FRET (Förster Resonance Energy Transfer) assays were carried out, using two fluorescent probes, proflavine (acting as the energy donor) included in the first ODA layer, and Nile Red (energy acceptor) in the DPPC outer layer (structures in Figure 4).

Figure 2. Chemical structure of Proflavine and Nile Red probes.

Förster resonance energy transfer (FRET) occurs when a donor fluorophore in the excited state transfers energy to an acceptor moiety in the ground state in a non-radiative process. FRET efficiency is defined as the proportion of donor molecules that have transferred their excess energy to acceptor molecules. Experimentally, as previously reported, it can be calculated by taking the ratio of the donor integrated fluorescence intensities in the presence of acceptor (FDA) and the absence of acceptor (F_D), following equation 1 [17],

$$\Phi_{FRET} = 1 - \frac{F_{DA}}{F_D} \quad (1)$$

The values of FRET efficiency, in turn, allow to calculate the distance between the donor molecules and the acceptor ones (equation 2) [17],

$$r_{AD} = R_0 \left[\frac{1-\Phi_{FRET}}{\Phi_{FRET}}\right]^{1/6} \quad (2)$$

Preprints (www.preprints.org) | NOT PEER-REVIEWED | Posted: 6 April 2022 doi:10.20944/preprints202204.0041.v1

where R_0 is the Förster radius (critical distance), that can be obtained by the spectral overlap, J(λ), between the donor emission and the acceptor absorption, according to the following relations (equation 3 and equation 4, with R_0 in Å, λ in nm, $\varepsilon_A(\lambda)$ in M^{-1} cm^{-1}):

$$R_0 = 0.2108\,[k^2\,\Phi_D^0\,n^{-4}\,J(\lambda)]^{1/6} \quad (3)$$

$$J(\lambda) = \int_0^\infty I_D(\lambda)\varepsilon_A(\lambda)\lambda^4 d\lambda \quad (4)$$

where $k^2 = 2/3$ is the orientational factor assuming random orientation of the dyes, Φ_D^0 is the fluorescence quantum yield of the donor in the absence of energy transfer, n is the refraction index of the medium, $I_D(\lambda)$ is the fluorescence spectrum of the donor normalized so that $\int_0^\infty I_D(\lambda)d\lambda = 1$, and $\varepsilon_A(\lambda)$ is the molar absorption coefficient of the acceptor.

The fusion ability of magnetoliposomes with membranes was assessed using giant unilamellar vesicles (GUVs) as membrane models, as previously reported [11]. GUVs were obtained from soybean lecithin (Sigma-Aldrich, St. Louis, MO, USA). First, 300 µL of soybean lecithin (1 mM) in chloroform were evaporated under an ultrapure nitrogen stream, until a thin film was obtained. Then, the film was pre-hydrated with 80 µL of deionized water and incubated at 45 °C for 30 minutes. After this period, 6 mL of an aqueous solution of glucose (6×10^{-4} M) was added and incubated at 37 °C for two hours [18]. Finally, the solution was centrifuged for 30 minutes at 10,000 rpm and the supernatant was collected, discarding the pellet of lipid aggregates.

2.3. Sedimentation curves of nanoparticles

The colloidal stability of the nanoparticles is an important parameter for biomedical applications. Hence, the sedimentation profile of suspensions of the prepared nanoparticles is crucial in determining their stability. The experimental results at different concentrations were fitted to the Becquerel's decay function (or Becquerel's decay law), which is given by equation (5),

$$I(t) = \frac{1}{[1+ct/\tau_0]^{1/c}} \quad , \quad (5)$$

where the control parameter c is taken as $0 < c < 1$, and τ_0 has dimensions of time [19].

2.4. Characterization techniques

The magnetic properties of nanoparticles were determined in a MPMS3 SQUID magnetometer MPMS5XL (Quantum Design Inc., San Diego, CA, USA), using applied magnetic fields up to 5 T. The magnetization dependence on magnetic field (hysteresis cycles) was performed by measuring the magnetization at a series of different applied magnetic fields, at room temperature.

Scanning Electron Microscopy images were recorded using a NanoSEM-FEI Nova 200 (FEI Technologies, Inc., Hillsboro, OR, USA), operating in transmission mode (STEM). ImageJ software (National Institutes of Health (NIH), version 1.53c, Bethesda, MD, USA) was used to process STEM images by increasing contrast and subtracting background.

The hydrodynamic diameter and zeta potential were measured using a Dynamic Light Scattering NANO ZS Malvern Zetasizer (Malvern Panalytical Ltd., Malvern, UK), that is equipped with a He-Ne laser (λ = 632.8 nm). For each sample, five independent measurements were carried out, to determine mean size and size distribution (polydispersity index).

2.5. Photophysical study of the antitumor compound in solution

The absorption and fluorescence properties of the antitumor compound were studied in several solvents, using 5×10^{-6} M compound solutions. Prior to measurements, the solutions were deaerated by a stream of nitrogen for 30 minutes. The fluorescence quantum yields were determined using as reference a solution of 1 ppm quinine sulfate in 0.05 M

Preprints (www.preprints.org) | NOT PEER-REVIEWED | Posted: 6 April 2022 doi:10.20944/preprints202204.0041.v1

sulfuric acid (Φ_r = 0.546 at 25 °C) [20], following the classic standard method (equation 6) [21,22],

$$\Phi_S = \left[\frac{A_r F_S n_S^2}{A_S F_r n_r^2}\right] \Phi_r \quad (6)$$

where A is the absorbance value at the excitation wavelength, F is the integrated emission spectral area, and n is the refractive index of the solvent used. The subscript r refers to the reference and the subscript s refers to the sample.

Spectroscopic-grade solvents and ultrapure water of Milli-Q grade (MilliporeSigma, St. Louis, MO, USA) were used in all preparations. The UV-Vis-NIR spectrophotometer Shimadzu UV-3600 Plus (Shimadzu Corporation, Kyoto, Japan) was used to measure the absorption spectra and the spectrofluorimeter Fluorolog 3 (HORIBA Jobin Yvon IBH Ltd., Glasgow, UK), with double monochromators in excitation and emission, was used to measure the emission spectra.

2.6. Encapsulation efficiency of compound in magnetoliposomes

The new antitumor thienopyridine was encapsulated into the magnetoliposomes by co-injection of the compound with the lipid solution, described as an efficient method for encapsulation of hydrophobic compounds [23].

The encapsulation efficiency, EE(%), of the antitumor compound in the magnetoliposomes was determined by using Amicon® Ultra centrifugal filter units 100 kDa (Merck Millipore, Darmstadt, Germany) for the separation of encapsulated and non-encapsulated compound. For that, drug loaded magnetoliposomes were subjected to a 60 min centrifugation at 11,000 rpm and the filtrate (consisting of non-encapsulated drug) fluorescence was measured. Then, the concentration of non-encapsulated compound was determined through a previously obtained calibration curve for each compound. The fluorescence intensity was measured and converted to the corresponding compound concentration. For each lipid formulation, three independent measurements were carried out and EE(%) was determined using equation (7),

$$EE(\%) = \frac{C_{(total\ compound)} - C_{(non-encapsulated\ compound)}}{C_{(total\ compound)}} \times 100 \quad (7)$$

2.7. Compound release assays

0.5 mL of drug-loaded magnetoliposomes solution was placed in Amicon® Ultra-0.5 mL centrifugal filters with 0.1 μm pore size, under mild shaking conditions, containing a GUVs solution in the bottom container, with GUVs being used as acceptor membrane models. At 30 min intervals (for 4.5 h), 200 μL were collected from the acceptor compartment for assessing compound concentration, and an equal volume of fresh GUVs was added. The release was assessed without alternating magnetic field (AMF) and under the actuation of an AMF. The AMF was generated in a custom-designed solenoid device (800 turns per meter, length 31 cm and internal diameter of 4.8 cm), by applying an alternating electric current. A magnetic field of 2.4 mT with a frequency of 1000 kHz was used. Release profile assays were performed in triplicate.

The fluorescence intensity of all aliquots was measured, and the release kinetics were fitted to the Korsmeyer-Peppas model (equation 8) [24],

$$\frac{C_t}{C_0} = K\, t^n \quad (8)$$

where C_t and C_0 are the concentrations at time t and 0, respectively, K is the release rate, t is the time and n is the transport exponent. The release mechanism depends on the value of the transport exponent, being defined by diffusion when $n < 0.45$; if $0.45 < n < 0.89$, release is controlled by relaxation; and when $n > 1$ it is controlled by swelling and relaxation of the system [25].

Preprints (www.preprints.org) | NOT PEER-REVIEWED | Posted: 6 April 2022 doi:10.20944/preprints202204.0041.v1

The Weibull model was also used [26],

$$m = 1 - \exp\left[\frac{-(t-T_i)^b}{a}\right] \quad (9)$$

where a is a parameter defining the timescale of the process, T_i a location parameter representing the latency time of the release mechanism (considered zero many times), t the time and b denotes the curve type shape parameter.

2.8. Magnetic hyperthermia

The heating and cooling curves were obtained using a magneTherm equipment from nanoTherics (Warrington, UK), using three different frequencies (f = 161 kHz, 270 kHz, and 381 kHz) and two field amplitudes (H = 16 mT and 17 mT). Before starting the measurement, the temperature of the sample was stabilized and then the alternating field was applied, and the temperature was recorded for a period of 30 minutes. Then, the applied field was turned off and the cooling of the samples was recorded for 30 minutes. These tests allowed the calculation of the specific absorption rate (SAR) and the intrinsic loss power (ILP), two parameters that indicate the ability of nanoparticles to generate heat in the presence of an external magnetic field. The SAR is defined as the amount of energy absorbed by the sample, per unit of mass (W/g), and can be obtained by equation 10,

$$SAR = C \times \frac{\Delta T}{\Delta t} \times \frac{m_s}{m_m} \quad (10)$$

where C is the specific heat capacity of suspension, $\frac{\Delta T}{\Delta t}$ is the initial slope of the curve, and m_s and m_m express the mass of suspension and magnetic material content in suspension, respectively.

Even though SAR is the most used parameter to characterize the heat capability generation, it doesn't allow comparing different experimental setups, because SAR value strongly depends on the strength and frequency of the AC applied field. Instead, intrinsic loss power (ILP, nH m²/kg) has been suggested and is given by equation 11,

$$ILP = \frac{SAR}{H^2 f} \quad (11)$$

where H is the field strength in kA/m, f is the frequency in kHz, and SAR should be introduced in W/kg [27].

3. Results and Discussion

3.1. Characterization of the multicore nanoparticles

The produced multicore nanoparticles were characterized by different techniques to evaluate their size, shape, stability and magnetic properties. The single manganese ferrite nanoparticles, prepared exactly by the same method used here, were previously described and characterized [4,11].

The UV-Visible absorption spectra were obtained for each of the prepared samples, using carboxymethyl-dextran (samples A1 and A2) and using melamine (sample B). The results are shown in figure 5.

 doi:10.20944/preprints202204.0041.v1

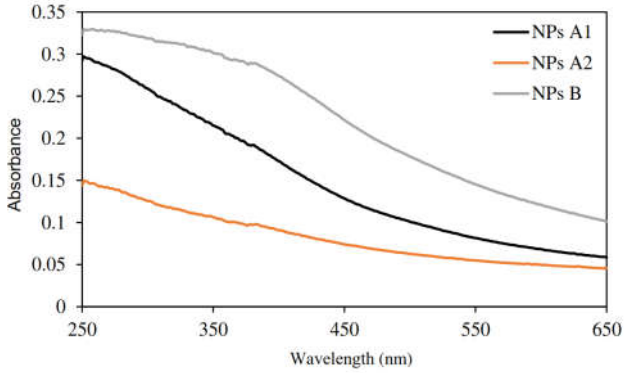

Figure 3. Absorption spectra of multicore nanoparticles A1, A2 and B.

A broad absorption spectrum was observed for all types of nanoparticles, with a band between 350 and 450 nm being visible in nanoparticles B, prepared with melamine.

The sedimentation of nanoparticles is governed by an initial first-order kinetics, followed by a decrease in the deposition rate. The sedimentation rates (k) of the nanoparticles were obtained by fitting the Becquerel function to the experimental data. This study was carried out for three different concentrations of nanoparticles, 0.025% (m/v), 0.05%, and 0.2% and the results obtained are shown in table 1.

Table 1. Sedimentation rates (k) calculated by the Becquerel function for nanoparticles A1, A2 and B.

Concentration (% m/v)	k (min^{-1})		
	NPs A1	NPs A2	NPs B
0.025	0.0011	0.0008	0.0017
0.05	0.0016	0.0008	0.0017
0.2	0.0034	0.0009	0.0021

It was observed that, for all samples, the sedimentation rate increases for higher values of NPs concentration. In general, A1 and A2 nanoparticles are more stable, presenting a lower sedimentation rate than B NPs. Among the nanoparticles A, a lower sedimentation rate is observed in sample A2, which indicates that the addition of the polysaccharide before the ferrite synthesis allows obtaining more stable nanoparticles. The type of flower-like structures obtained from the different methods can be the determining factor for colloidal stability.

The magnetic properties of nanoparticles A1, A2 and B were evaluated in a SQUID instrument. This technique allows studying the dependence of the magnetic moment as a function of an applied field through hysteresis curves. Figure 6 displays the hysteresis curves of the three synthesized nanoparticles. The values of coercivity, remnant magnetization, saturation magnetization and the ratio between remnant and saturation magnetization are summarized in table 2.

 doi:10.20944/preprints202204.0041.v1

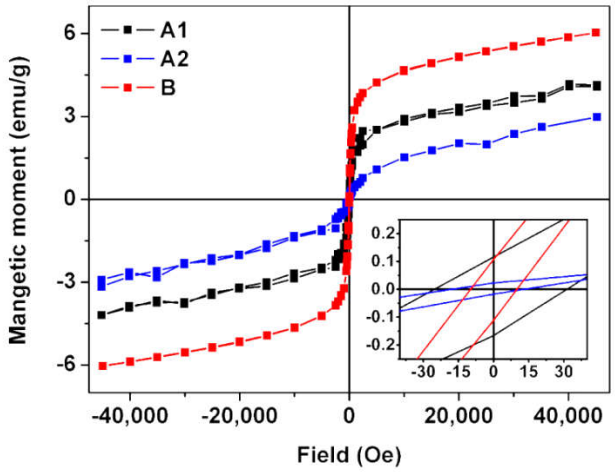

Figure 4. Hysteresis curve of the multicore manganese ferrite nanoparticles A1, A2 and B, at room temperature. Insert: Magnification of the low-field zone of the hysteresis curves.

Table 2. Values of coercivity, remanence magnetization, saturation magnetization and ratio between remnant magnetization and saturation magnetization (M_r/M_s), obtained from hysteresis curves, for the several nanoparticles.

	Coercivity (Oe)	Remnant magnetization (emu/g)	Magnetization of saturation (emu/g)	M_r/M_s
A1	25.12	0.12	4.30	0.03
A2	9.34	0.02	3.20	0.01
B	16.23	0.11	6.16	0.02

For all the prepared nanoparticles, it is possible to verify that the values of the ratio between the remnant and saturation magnetization corroborate the superparamagnetic behavior of the NPs, presenting values below 0.1 that indicate the loss of more than 90% of the magnetization after removal of the field applied [28].

Nanoparticles A showed similar magnetization values of 4.30 emu/g and 3.20 emu/g for A1 and A2, respectively. However, A1 nanoparticles show higher hysteresis, with higher coercivity and remnant values than those obtained for A2 nanoparticles. Nanoparticles B had the highest magnetization value of 6.16 emu/g. Low saturation magnetization values are common in this type of multicore structures, as reported by Lu *et al.* [29].

The assessment of the shape and size of multicore manganese ferrite nanoparticles was performed by SEM technique. Despite some agglomeration, it is possible to observe the generally spherical shape of the nanoparticles (figure 7).

Preprints (www.preprints.org) | NOT PEER-REVIEWED | Posted: 6 April 2022 doi:10.20944/preprints202204.0041.v1

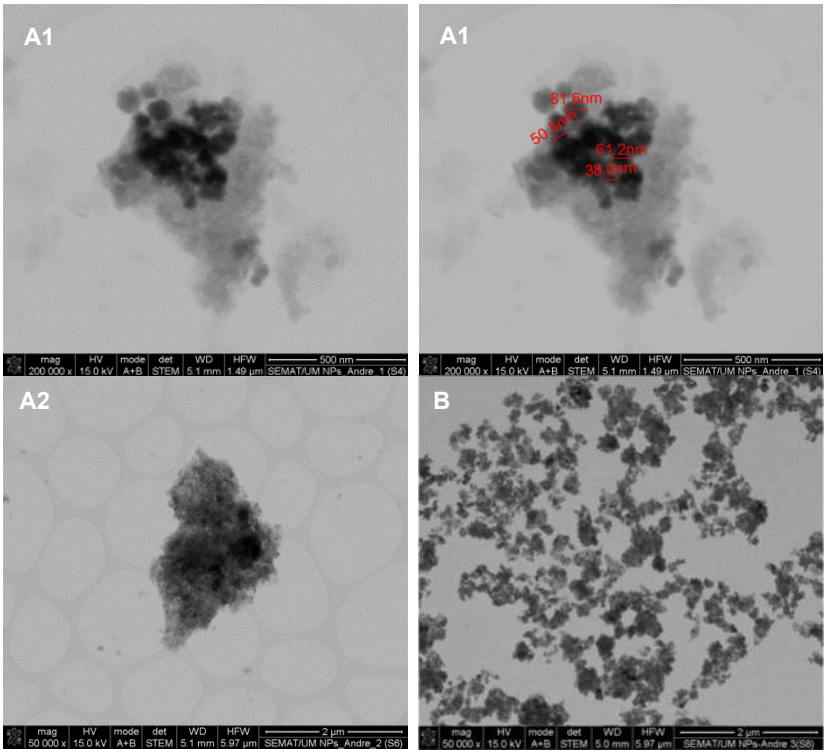

Figure 7. STEM images of multicore nanoparticles from samples A1 (in the right with the indication of aggregates size), A2 and B.

The analysis by SEM (in transmission mode, STEM) allowed concluding that there was no formation of flower-like structures for nanoparticles A1 and A2, despite the observation of aggregates. This was not expected, since the use of carboxymethyl-dextran has been reported to generate this kind of structures in iron oxide nanoparticles, with aggregates from 20 to 30 nm [5,6].

On the other hand, sample B revealed well-defined flower-like structures. Figure 7B was analyzed with ImageJ software, and selected flower-shaped structures were selected (35 counts). The areas obtained were converted into diameters, and the results adjusted to the sum of two Gaussians, allowing the distribution of sample sizes to be obtained. Two populations were obtained 203 ± 37 nm and 311 ± 35 nm (figure 8).

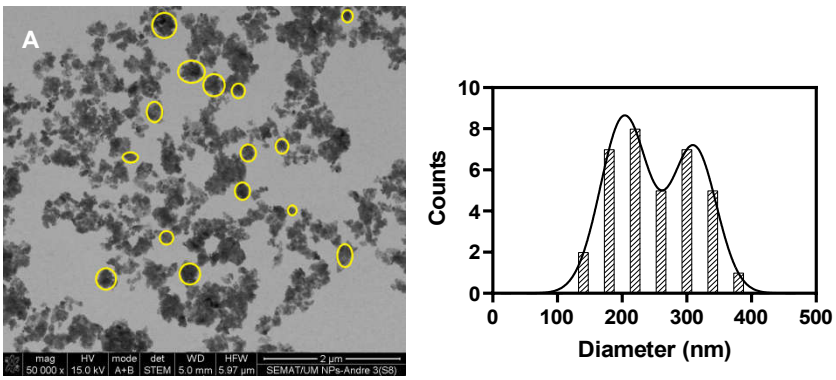

Preprints (www.preprints.org) | NOT PEER-REVIEWED | Posted: 6 April 2022 doi:10.20944/preprints202204.0041.v1

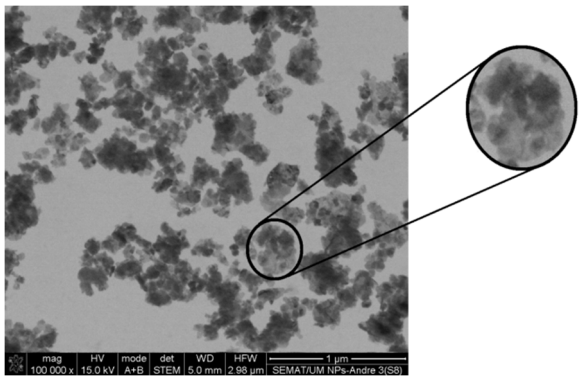

Figure 8. SEM images of sample B at different magnifications. A: Manual identification of various flower-like structures and corresponding size histogram fitted to the sum of two Gaussian distributions. B: Identification and enlargement of a flower-shaped structure.

Considering the results obtained, nanoparticles B were selected for magnetic hyperthermia assays. The heating and cooling curves were obtained using three different frequencies and two field amplitudes. Before starting the measurement, the temperature of the sample was stabilized and then the alternating field was applied. The results obtained are shown in figure 9.

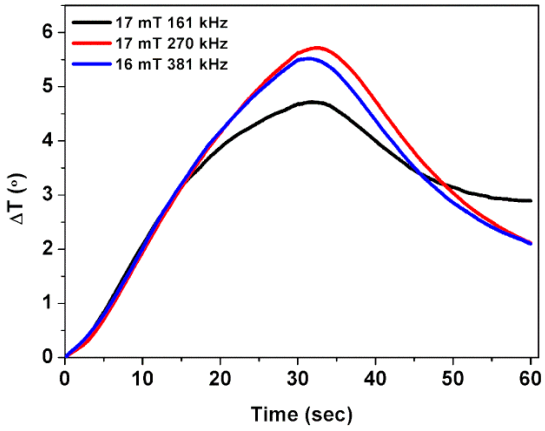

Figure 9. Temperature variation of nanoparticles B, in the presence of alternating magnetic fields of amplitude 17 mT with frequencies of 161 kHz and 270 kHz, and 16 mT with frequency of 381 kHz.

It is observed an increase between 4 and 6 °C, in 30 minutes, for the several experimental conditions. The largest heating was observed for the 17 mT field with a frequency of 270 kHz. Table 3 shows the SAR and ILP values calculated for the three experimental conditions.

Table 3. SAR and ILP values, obtained from the heating and cooling curves of nanoparticles B.

	17 mT/161 kHz	**17 mT/270 kHz**	**16 mT/381 kHz**
SAR (W/g)	0.12	0.10	0.14
ILP (nH.m²/kg)	0.46	0.20	0.22

S

The values obtained indicate a higher SAR value of 0.14 W per g of neat nanoparticles (mass of $MnFe_2O_4$) for the 16 mT field with a frequency of 381 kHz. On the other hand, a

Preprints (www.preprints.org) | NOT PEER-REVIEWED | Posted: 6 April 2022 doi:10.20944/preprints202204.0041.v1

higher ILP was obtained for the 17 mT and 161 kHz field. ILP values between 0.1 and 0.58 have been reported for manganese-doped spherical ferrites [30]. Thus, the values obtained are expected for this type of nanoparticles. These data indicate that the NPs obtained have a good heating capability due to their flower-like structure. It is concluded that the NPs produced have suitable characteristics for application in magnetic hyperthermia therapeutic approaches, while the superparamagnetic behavior avoids aggregation when the applied magnetic field is removed [31,32].

3.2. Magnetoliposomes characterization

Förster resonance energy transfer (FRET) was used as proof of the formation of the double layer of MLs membrane, considering the novelty of these nanosystems containing multicore nanoparticles. For that, proflavine was used as energy donor, and was included before adding the first ODA layer, while the lipid probe Nile Red was incorporated in the outer lipid layer. For comparison, similar systems were prepared with only proflavine and with only Nile Red. The spectra of the three samples (figure 10) were measured exciting only the donor proflavine.

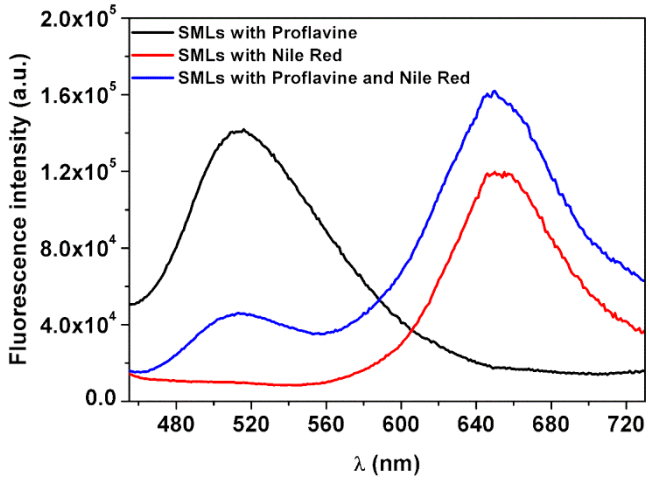

Figure 10. Fluorescence spectra (λ_{exc} = 380 nm) of MLs (based on nanoparticles B) containing only proflavine (5×10^{-6} M), only Nile Red (5×10^{-6} M) and containing both fluorophores.

Comparing the spectrum of proflavine in MLs with the spectrum of systems containing the two probes, it is possible to observe a decrease in the donor band (at ~510 nm) for systems containing the acceptor (Nile Red). Thus, the increase in the fluorescence intensity of the acceptor band (at ~660 nm) and the consequent decrease in the fluorescence intensity of the donor, confirms the existence of FRET between the two fluorescent probes. Considering that FRET only occurs at donor-acceptor distances below 10 nm, it is possible to confirm the formation of the bilayer around the nanoparticles and, consequently, the synthesis of magnetoliposomes. This study allowed to calculate the FRET efficiency, the Förster radius and the distance between the donor and acceptor (equations 1 to 4). The results obtained are shown in the table 4.

Table 4. Förster energy transfer parameters, FRET efficiency (Φ_{FRET}), Förster radius (R_0) and donor-acceptor distance (r) obtained.

	Φ_{FRET} (%)	R_0 (Å)	r (Å)
MLs	68	13.6	12

A high FRET efficiency of 68% was calculated, with a corresponding donor-acceptor distance of 1.2 nm. Given that the donor is attached to the surface of the flower-shaped

 doi:10.20944/preprints202204.0041.v1

structures and that the acceptor probe is added immediately before the second lipid layer formed by DPPC, which has a typical size of about 3.9 nm [28], the distance obtained supports the formation of a bilayer around the flower-shaped nanoparticles.

Magnetoliposomes (MLs) were prepared from A2 and B nanoparticles. Considering the importance of stability in solution, the MLs were subjected to sedimentation kinetics studies. The results obtained through the fit to the Becquerel equation are represented in table 5.

Table 5. Sedimentation rate (k) calculated by the Becquerel function of solid magnetoliposomes.

	Concentration % (m/v)	k (min^{-1})	
		NPs A2	NPs B
MLs	0.025	0.0023	0.0014
Only NPs		0.0008	0.0017

S

MLs based on A2 nanoparticles showed increased sedimentation rates relative to the NPs alone. On the other hand, MLs based on B nanoparticles showed a slight decrease, indicating that the encapsulation of these NPs in liposomes increases their stability. Thus, it is possible to conclude that the formation of well-defined flower-shaped structures, such as the ones of NPs B, allows the development of stable nanosystems.

To characterize the size and polydispersity (PDI) of the synthesized magnetoliposomes, dynamic light scattering (DLS) and SEM measurements were used. However, the DLS technique does not distinguish between the various types of particles, reporting only their effective size. The mean values of hydrodynamic diameter, polydispersity and zeta potential are summarized in table 6.

Table 6. Mean values and standard deviation of hydrodynamic diameter, polydispersity index (PDI) and zeta potential of magnetoliposomes based on multicore nanoparticles, obtained by DLS.

	Hydrodynamic diameter (nm)	PDI	Zeta Potential (mV)
MLs A2	330 ± 18	0.1 ± 0.02	-0.5 ± 0.4
MLs B	388 ± 22	0.2 ± 0.11	-2.4 ± 7.4

By analyzing the hydrodynamic diameter, sizes between 330 nm and 388 nm are observed, the MLs based on nanoparticles B (synthesized with melamine) exhibiting the largest size values. This can be justified by the flower-shaped structures of nanoparticles B, as confirmed by the SEM analysis. Polydispersity index values lower than 0.2 for all samples indicate homogeneous populations for the developed MLs. Regarding the surface charge, the nanosystems show a neutral to very slightly negative zeta potential. The lipid of the outer layer of the MLs, DPPC, is a zwitterionic lipid. Thus, the zeta potential of the magnetoliposomes is in line with the expected, given the globally neutral charge of this lipid.

The characterization of the sizes and shape of the prepared MLs was further evaluated by SEM (figure 11). It is possible to observe MLs with a spherical shape, with measured sizes between 240 nm (nanoparticles A2) and 265 nm (nanoparticles B). The structure of ~ 441 nm can be an aggregate of two MLs. Overall, SEM results agree with the data

Preprints (www.preprints.org) | NOT PEER-REVIEWED | Posted: 6 April 2022 doi:10.20944/preprints202204.0041.v1

obtained by DLS technique, considering that DLS measures hydrodynamic diameters (while in SEM we have dry samples) and that some aggregation can take place in solution.

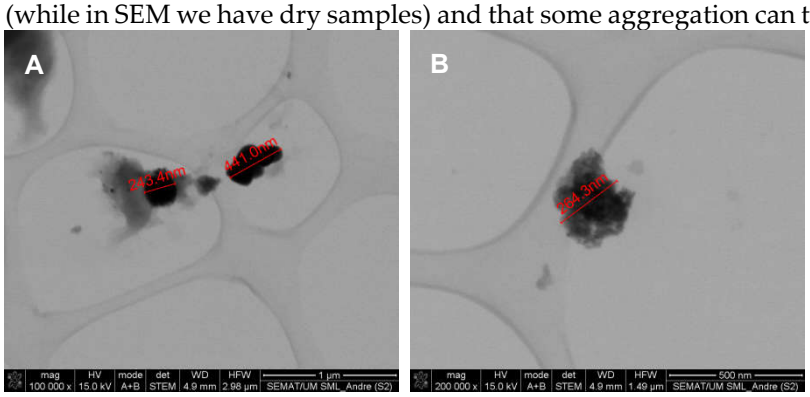

Figure 7. SEM images of magnetoliposomes based on A2 nanoparticles (A) and B nanoparticles (B).

The study of the interaction of magnetoliposomes with models of cell membranes is essential to assess their fusion ability. This study is based on the emission quenching phenomenon, derived from the proximity between the fluorophore and the magnetic NPs. The quenching processes can be a photoinduced electron transfer or an increase in intersystem crossing process by heavy atom effect or energy transfer to the nanoparticles. After interaction with giant unilamellar vesicles (GUVs), an increase in fluorescence emission is detected, due to the decrease in quenching promoted by the NPs, indicating that MLs of multicore nanoparticles also have a fusion capability, similarly to that previously reported for $MnFe_2O_4$-based magnetoliposomes [4,11].

3.3. Drug-loaded magnetoliposomes

The fluorescent antitumor thienopyridine derivative was previously synthesized [12]. The UV-Visible absorption and fluorescence spectra were measured in several solvents with different polarities and results are shown in figure 12.

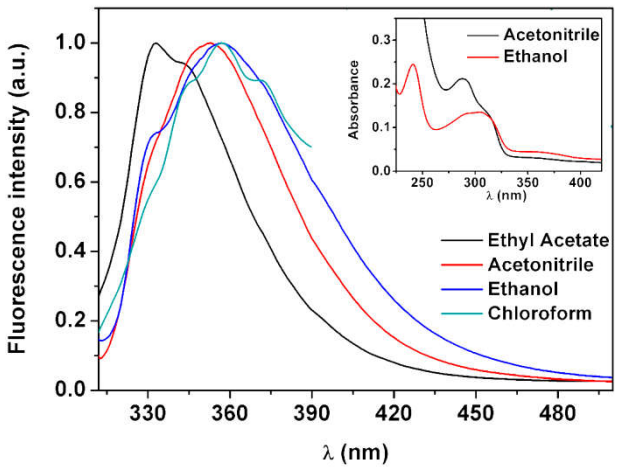

Figure 12. Normalized fluorescence spectra of the antitumor thienopyridine derivative (5×10^{-6} M) (λ_{exc}=300 nm) in several solvents. Inset: Absorption spectra of compound (1×10^{-5} M) in ethanol and ethyl acetate.

The antitumor compound demonstrates reasonable fluorescence in all solvents. A general redshift of the emission band with increasing polarity is detected, together with a loss of vibrational structure, which can be explained by an intramolecular charge transfer character of the excited state and/or specific interactions with polar solvents [17]. This behavior is similar to the observed for other thieno[3,2-*b*]pyridine-based compounds, with antitumor and/or antiangiogenic properties, previously synthesized and studied [33-37].

 doi:10.20944/preprints202204.0041.v1

The maximum absorption and emission wavelengths, molar absorption coefficients, and fluorescence quantum yield values are shown in table 7.

Table 7. Maximum absorption wavelengths (λ_{abs}), molar absorption coefficients (ε), maximum emission wavelengths (λ_{em}) and fluorescence quantum yields of the antitumor compound.

Solvent	λ_{abs}/nm ($\varepsilon/10^4$ $M^{-1}cm^{-1}$)	λ_{em} (nm)	Φ_F
Ethyl acetate	288 (1.1)	333	0.04
Acetonitrile	301 (0.7)	353	0.03
Ethanol	305 (0.7)	357	0.03

This preliminary photophysical study allows us to determine the encapsulation efficiency and to follow the drug release profile using the fluorescence emission of the antitumor compound.

Encapsulation efficiency is a key factor in the development of a drug nanocarrier. In this way, the compound encapsulation efficiency (from three independent assays) in MLs of nanoparticles B was determined as 98% ± 2.6% (using equation 7), thus being very high. This result indicates that MLs are excellent encapsulation systems for the magnetically-guided transport of this antitumor compound. Thus, these MLs are promising for cancer therapy as therapeutic agents for chemotherapy and magnetic hyperthermia.

The compound release assays from the MLs were performed and the results of the cumulative release over time are shown in figure 13. The release profiles, obtained for 10 hours, are quite similar for the absence and presence of an alternating magnetic field (AMF) of low intensity (H=2.4 mT, f=1 MHz), despite the release is slightly higher in the presence of AMF. In fact, the application of the AMF did not have the expected rise in compound release. This can be due to several factors (that can be conjugated): the compound is very hydrophobic, hampering a large release to an aqueous media; the concentration used of magnetic nanoparticles was very low; more time is needed to attain an appreciable release under the application of AMF; the applied AMF was too weak to cause the needed temperature rise and promote release from the DPPC layer (this lipid is rigid at room temperature and phase transition temperature is at 41 °C [38]).

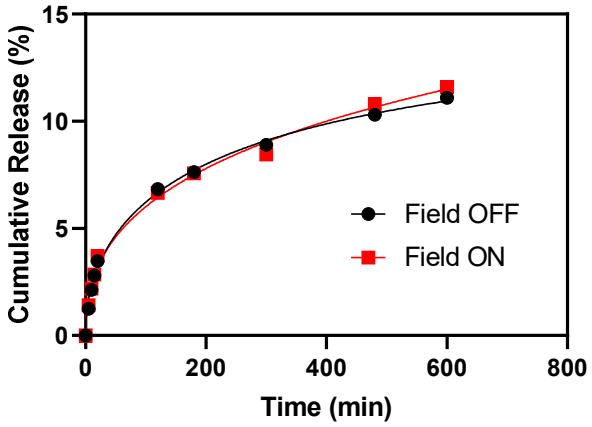

Figure 13. Release profile of compound encapsulated in MLs in the presence and absence of an applied magnetic field, fitted to the Weibull model.

Nevertheless, the fitting to Korsmeyer-Peppas and Weibull models is of good quality and the parameters are displayed in table 8. It is possible to observe a burst release in the first 30 minutes, followed by a slower release until the end of the assays.

 doi:10.20944/preprints202204.0041.v1

Table 8. Parameters obtained by fitting to the Korsmeyer-Peppas and Weibull models, and the respective coefficient of determination (R^2), of release assays in the presence and absence of an applied magnetic field.

	Korsmeyer-Peppas			Weibull		
	K (min^{-1})	n	R^2	a	b	R^2
No Field	0.012	0.34	0.979	0.052	0.52	0.997
With Field	0.013	0.35	0.975	0.029	0.42	0.994

The fitting to the Korsmeyer-Peppas model indicates a transport by diffusion ($n < 0.45$). The same indication is provided by the Weibull model, considering the values of the b parameter lower than 0.75 [26]. From this model, it was also possible to estimate a maximum compound release of 31.9% in the presence of the applied field, about twice the predicted in the absence of magnetic field (14.3%). Thus, the magnetoliposomes developed are a promising nanosystem for the controlled and sustained release of the antitumor compound in the presence of an AMF, allowing the combination of chemotherapy and magnetic hyperthermia.

Author Contributions: Conceptualization, A.R.O.R., P.J.G.C. and E.M.S.C.; methodology, A.R.O.R., M.J.R.P.Q. and E.M.S.C.; validation, A.R.O.R., B.G.A., A.M.P., J.P.A. and E.M.S.C.; formal analysis, F.A.C.L., A.V.F.F., J.M.R., A.M.P., J.P.A.; investigation, F.A.C.L., A.V.F.F., J.M.R., A.P., B.G.A.; writing—original draft preparation, F.A.C.L. and E.M.S.C.; writing—review and editing, A.R.O.R.; P.J.G.C.; E.M.S.C.; supervision, A.R.O.R., A.M.P., J.P.A., M.J.R.P.Q. and P.J.G.C.; project administration, P.J.G.C. All authors have read and agreed to the published version of the manuscript.

Institutional Review Board Statement: Not applicable.

Informed Consent Statement: Not applicable.

Data Availability Statement: Not applicable.

Funding: This research was funded by the Portuguese Foundation for Science and Technology (FCT) in the framework of the Strategic Funding of CF-UM-UP (UIDB/04650/2020) and through the research project PTDC/QUI-QFI/28020/2017 (POCI-01-0145-FEDER-028020), financed by the European Fund of Regional Development (FEDER), COMPETE2020, and Portugal2020. J.M.R. acknowledges FCT, ESF (European Social Fund—North Portugal Regional Operational Program) and HCOP (Human Capital Operational Program) for a PhD grant (SFRH/BD/115844/2016).

Conflicts of Interest: The authors declare no conflict of interest.

References

1. World Health Organization (WHO). Cancer. https://www.who.int/health-topics/cancer#tab=tab_1 (accessed Mar 23, 2022).
2. Yang, H.; Zhang, C.; Shi, X.; Hu, H.; Du, X.; Fang, Y.; Ma, Y.; Wu, H.; Yang, S. Water-Soluble Superparamagnetic Manganese Ferrite Nanoparticles for Magnetic Resonance Imaging. *Biomaterials* **2010**, *31*, 3667–3673. doi:10.1016/j.biomaterials.2010.01.055
3. Pradhan, P.; Giri, J.; Banerjee, R.; Bellare, J.; Bahadur, D. Preparation and Characterization of Manganese Ferrite-Based Magnetic Liposomes for Hyperthermia Treatment of Cancer. *Journal of Magnetism and Magnetic Materials* **2007**, *311*, 208–215. doi:10.1016/j.jmmm.2006.10.1179
4. Rodrigues, A.R.O.; Ramos, J.M.F.; Gomes, I.T.; Almeida, B.G.; Araújo, J.P.; Queiroz, M.-J.R.P.; Coutinho, P.J.G.; Castanheira, E.M.S. Magnetoliposomes based on manganese ferrite nanoparticles as nanocarriers for antitumor drugs. *RSC Advances* **2016,** *6*, 17302-17313; doi:10.1039/C5RA27058H
5. Gavilán, H.; Kowalski, A.; Heinke, D.; Sugunan, A.; Sommertune, J.; Varón, M.; Bogart, L. K.; Posth, O.; Zeng, L.; González-Alonso, D.; Balceris, C.; Fock, J.; Wetterskog, E.; Frandsen, C.; Gehrke, N.; Grüttner, C.; Fornara, A.; Ludwig, F.; Veintemillas-Verdaguer, S.; Johansson, C.; Morales, M. P. Colloidal Flower-Shaped Iron Oxide Nanoparticles: Synthesis Strategies and Coatings. *Particle & Particle Systems Characterization* **2017**, *34*, 1700094. doi:10.1002/ppsc.201700094
6. Dutz, S. Are Magnetic Multicore Nanoparticles Promising Candidates for Biomedical Applications? *IEEE Transactions on Magnetics* **2016**, *52*, 0200103. doi:10.1109/TMAG.2016.2570745
7. Shubitidze, F.; Kekalo, K.; Stigliano, R.; Baker, I. Magnetic nanoparticles with high specific absorption rate of electromagnetic energy at low field strength for hyperthermia therapy. *J. Appl. Phys.* **2015**, *117*, 094302. doi: 10.1063/1.4907915

8. Chen, Y.; Bose, A.; Bothun, G. D. Controlled Release from Bilayer-Decorated Magnetoliposomes via Electromagnetic Heating. *ACS Nano* **2010**, *4*, 3215-3221. doi: 10.1021/nn100274v
9. Nappini, S.; Bonini, M.; Bombelli, F. B.; Pineider, F.; Sangregorio, C.; Baglioni, P.; Nordèn, B. Controlled Drug Release under a Low Frequency Magnetic Field: Effect of the Citrate Coating on Magnetoliposomes Stability. *Soft Matter* **2011**, *7*, 1025-1037. doi: 10.1039/C0SM00789G
10. Peetla, C.; Stine, A.; Labhasetwar, V. Biophysical Interactions with Model Lipid Membranes: Applications in Drug Discovery and Drug Delivery. *Molecular Pharmaceutics* **2009**, *6*, 1264-1276. doi:10.1021/mp9000662
11. Rodrigues, A.R.O.; Almeida, B.G.; Rodrigues, J.M.; Queiroz, M.-J.R.P.; Calhelha, R. C.; Ferreira, I.C.F.R.; Pires, A.; Pereira, A.M.; Araújo, J.P.; Coutinho, P.J.G.; Castanheira, E.M.S. Magnetoliposomes as carriers for promising antitumor thieno[3,2-*b*]pyridin-7-arylamines: photophysical and biological studies. *RSC Advances* **2017**, *7*, 15352-15361. doi:10.1039/c7ra00447h
12. Rodrigues, J. M.; Calhelha, R. C.; Ferreira, I. C. F. R.; Queiroz, M.-J. R. P. Application of PEG_{400} in the one-pot synthesis of 7-[4-alkyl- or (hetero)aryl-1*H*-1,2,3-triazol-1-yl]thieno[3,2-*b*]pyridines via S_NAr and Cu(I)-catalyzed Azide-Alkyne Cycloaddition and preliminary evaluation of their anti-tumour activity. *Tetrahedron Letters* **2020**, *61*, 151900. doi:10.1016/j.tetlet.2020.151900
13. Han, D.; Han, S.-Y.; Lee, N. S.; Shin, J.; Jeong, Y. G.; Park, H.-W.; Kim, D. K. Magnetofluorescent Nanocomposite Comprised of Carboxymethyl Dextran Coated Superparamagnetic Iron Oxide Nanoparticles and β-Diketon Coordinated Europium Complexes. *Nanomaterials* **2019**, *9*, 62. doi:10.3390/nano9010062
14. Woodman, E. K.; Chaffey, J. G.; Hopes, P. A.; Hose, D. R.; Gilday, J. P. *N,N'*-Carbonyldiimidazole-mediated amide coupling: Significant rate enhancement achieved by acid catalysis with imidazole·HCl. *Organic Process Research & Development* **2008**, *13*, 106-113. doi:10.1021/op800226b
15. Padiya, K. J.; Gavade, S.; Kardile, B.; Tiwari, M.; Bajare, S.; Mane, M.; Gaware, V.; Varghese, S.; Harel, D.; Kurhade, S. Unprecedented "in water" Imidazole Carbonylation: Paradigm Shift for Preparation of Urea and Carbamate. *Org. Lett.* **2012**, *14*, 2814–2817, doi:10.1021/ol301009d
16. Rio, I.S.R.; Rodrigues, A.R.O.; Rodrigues, J.M.; Queiroz, M.-J.R.P.; Calhelha, R.C.; Ferreira, I.C.F.R.; Almeida, B.G.; Pires, A.; Pereira, A.M.; Araújo, J.P.; Castanheira, E.M.S.; Coutinho, P.J.G. Magnetoliposomes based on magnetic/plasmonic nanoparticles loaded with tricyclic lactones for combined cancer therapy. *Pharmaceutics* **2021**, *13*, 1905. Doi: 10.3390/pharmaceutics13111905
17. Valeur, B.; Molecular fluorescence - Principles and applications; Wiley-VCH: Weinheim, 2001.
18. Tamba, Y.; Terashima, H.; Yamazaki, M. A Membrane Filtering Method for the Purification of Giant Unilamellar Vesicles. *Chem. Phys. Lipids* **2011**, *164*, 351–358. doi: 10.1016/j.chemphyslip.2011.04.003
19. Foderà, V.; Donald, A. Tracking the heterogeneous distribution of amyloid spherulites and their population balance with free fibrils. *Eur. Phys. J. E* **2010**, *33*, 273–282. doi:10.1140/epje/i2010-10665-4
20. Eastman, J. W. Quantitative spectrofluorimetry – The Fluorescence quantum yield of quinine sulfate. *Photochemistry and Photobiology* **1967**, *6*, 55–72. doi: 10.1111/j.1751-1097.1967.tb08790.x
21. Crosby, G. A.; Demas, J. N. Measurement of Photoluminescence Quantum Yields. Review. *J. Phys. Chem.* **1971**, *75*, 991–1024. doi:10.1021/j100678a001
22. Fery-Forgues, S.; Lavabre, D. Are Fluorescence Quantum Yields so Tricky to Measure? A Demonstration Using Familiar Stationery Products. *J. Chem. Educ.* **1999**, *76*, 1260. Doi:10.1021/ed076p1260
23. Jaafar-Maalej, C.; Diab, R.; Andrieu, V.; Elaissari, A.; Fessi, H. Ethanol injection method for hydrophilic and lipophilic drug-loaded liposome preparation. *J. Liposome Res.* **2010**, *20*, 228-243. doi 10.3109/08982100903347923
24. Korsmeyer, R.W.; Gurny, R.; Doelker, E.; Buri, P. Peppas, N.A. Mechanisms of solute release from porous hydrophilic polymers, *Int. J. Pharm.* **1983**, *15*, 25-35.
25. Dash, S.; Murthy, P.N.; Nath, L.; Chowdhury, P. Kinetic modelling on drug release from controlled drug delivery systems. *Acta Pol. Pharm.*, **2010**, *67*, 217–223.
26. Papadopoulou,V.; Kosmidis, K.; Vlachou, M.; Macheras, P. On the use of the Weibull function for the discernment of drug release mechanisms. *Int. J. Pharm.* **2006**, *309*, 44-50. doi: 10.1016/j.ijpharm.2005.10.044
27. Kallumadil, M.; Tada, M.; Nakagawa, T.; Abe, M.; Southern, P.; Pankhurst, Q.A. Suitability of commercial colloids for magnetic hyperthermia. *J. Magn. Magn. Mater.* **2009**, *321*, 1509-1513. doi: 10.1016/j.jmmm.2009.02.075
28. Cardoso, B.D.; Rodrigues, A.R.; Almeida, B.G.; Amorim, C.O.; Amaral, V.S.; Castanheira, E.M.S.; Coutinho, P.J.G. Stealth Magnetoliposomes Based on Calcium-Substituted Magnesium Ferrite Nanoparticles for Curcumin Transport and Release. *Int. J. Molec. Sci.* **2020**, *21*, 3641. doi: 10.3390/ijms21103641
29. Lu, H. M.; Zheng, W. T.; Jiang, Q. Saturation Magnetization of Ferromagnetic and Ferrimagnetic Nanocrystals at Room Temperature. *J. Phys. D: Appl.Phys.* **2007**, *40*, 320–325. doi: 10.1088/0022-3727/40/2/006
30. Gupta, R.; Tomar, R.; Chakraverty, S.; Sharma, D. Effect of Manganese Doping on the Hyperthermic Profile of Ferrite Nanoparticles Using Response Surface Methodology. *RSC Advances* **2021**, *11*, 16942–16954. doi: 10.1039/D1RA02376D
31. Kekalo, K.; Baker, I.; Meyers, R.; Shyong, J. Magnetic Nanoparticles with High Specific Absorption Rate at Low Alternating Magnetic Field. *Nano Life* **2015**, *05*, 1550002. Doi: 10.1142/S1793984415500026

32. Shubitidze, F.; Kekalo, K.; Stigliano, R.; Baker, I. Magnetic Nanoparticles with High Specific Absorption Rate of Electromagnetic Energy at Low Field Strength for Hyperthermia Therapy. *J. Appl. Phys*. **2015**, *117*, 094302. doi:10.1063/1.4907915
33. Queiroz, M.-J.R.P.; Dias, S.; Peixoto, D.; Rodrigues, A.R.O.; Oliveira, A. D. S.; Coutinho, P. J. G.; Vale-Silva, L. A.; Pinto, E.; Castanheira, E. M. S. New Potential Antitumoral Di(Hetero)Arylether Derivatives in the Thieno[3,2-*b*]Pyridine Series: Synthesis and Fluorescence Studies in Solution and in Nanoliposomes. *J. Photochem. Photobiol. A: Chem.* **2012**, *238*, 71–80. Doi: 10.1016/J.JPHOTOCHEM.2012.04.007
34. Queiroz, M.-J.R.P.; Calhelha, R.C.; Vale-Silva, L.; Pinto, E.; Nascimento, M.S.-J. Novel [6-(hetero)arylamino]thieno[3,2-*b*] pyridines: synthesis and antitumoral activities. *Eur. J. Med. Chem.* **2010**, *45*, 5732-5738. doi:10.1016/j.ejmech.2010.09.030
35. Machado, V. A.; Peixoto, D.; Costa, R.; Froufe, H.J.C.; Calhelha, R.C.; Abreu, R.M.V.; Ferreira, I.C.F.R.; Soares, R.; Queiroz, M.-J.R.P. Synthesis, antiangiogenesis evaluation and molecular docking studies of 1-aryl-3-[(thieno[3,2-*b*]pyridin- 7-ylthio)phenyl]ureas: Discovery of a new substitution pattern for type II VEGFR-2 Tyr kinase inhibitors. *Bioorg. Med. Chem.* **2015**, *23*, 6497-6509. doi:10.1016/j.bmc.2015.08.010
36. Machado, V.A.; Peixoto, D.; Queiroz, M.-J.R.P.; Soares, R. Antiangiogenic 1-aryl-3-[3-(thieno[3,2-*b*]pyridin- 7-ylthio)phenyl]ureas inhibit MCF-7 and MDA-MB-231 human breast cancer cell lines through PI3K/Akt and MAPK/Erk pathways. *J. Cell. Biochem.* **2016**, *117*, 2791–2799. doi:10.1002/jcb.25580
37. Costa, C.N.C.; Hortelão, A.C.L.; Ramos, J.M.F.; Oliveira, A.D.S.; Calhelha, R.C.; Queiroz, M.-J.R.P.; Coutinho, P.J.G.; Castanheira, E.M.S. A new antitumoral heteroarylaminothieno[3,2-*b*]pyridine derivative: Incorporation in liposomes and interaction with proteins monitored by fluorescence. *Photochem. Photobiol. Sci.* **2014**, *13*, 1730-1740. doi:10.1039/C4PP00287C
38. Lentz, B.; Membrane 'fluidity' as detected by diphenylhexatriene probes. *Chem. Phys. Lipids* **1989**, *50*, 171-190. doi: 10.1016/0009-3084(89)90049-2